RESEARCH PAPER

Illumination spot profile correction in digital holographic microscopy for overlay metrology

Manashee Adhikary[a,b,*] **Tamar van Gardingen-Cromwijk**[a,b] **Jo de Wit**[c]
Stefan Witte[a,b] **Johannes F. de Boer**[a] **and Arie den Boef**[a,b,c]
^aVrije Universiteit, Department of Physics and Astronomy, and LaserLaB, Amsterdam, The Netherlands
^bAdvanced Research Center for Nanolithography (ARCNL), Amsterdam, The Netherlands
^cASML Netherlands B.V., Veldhoven, The Netherlands

ABSTRACT. **Background:** Precise, accurate, and fast overlay (OV) metrology is an important step in semiconductor device manufacturing. With the increasing demand for better OV over a larger range of different process layers, the optics used in OV metrology tools become more complex, bulky, and expensive. OV, which is to be measured with sub-nanometer precision, is susceptible to many small imperfections in the measurement system.

Aim: We present a dark-field digital holographic microscope (DHM) that measures the complex field of the OV targets using simple optics, followed by computational algorithms to correct for hardware imperfections. With the setup, we aim to correct the effects of the absolute intensity of the illumination beam as well as the spatial profile.

Approach: The spatial profiles of two oblique illumination beams for diffraction based OV metrology are calibrated using large gratings as calibration targets using DHM, and thereafter OV target images are corrected by the calibrated illumination spot profiles.

Results: OVs are calculated for test targets with known OV values, and illumination spot correction removes errors originating from intensity imbalance and intensity variation.

Conclusion: We present an optical OV measurement method that is more robust against non-uniform illumination beams using simple calibration steps.

1 Introduction

With the continued shrink of device feature sizes and more complex devices being developed, there has been a relentless push for significant semiconductor overlay (OV) metrology improvements for accurate, precise, and fast OV measurements with an accuracy of less than a nanometer (nm). Fast OV metrology is based on optical measurements systems, such as image based OV,[1] diffraction based OV (DBO),[2–4] and scatterometry.[5] As smaller OV targets with low diffraction efficiencies are used, the challenges to obtaining high-resolution imaging and high signal-to-noise ratios lead to demanding precision requirements on the optics in the metrology tool.

---

*Address all correspondence to Manashee Adhikary, m.adhikary@arcnl.nl

Moreover, to deal with various materials used in the chip stacks, OV metrology demands a broad wavelength range and tunable wavelengths, which increases the complexity of measurement systems.

To lower the complexity of the optics in OV metrology tools to acceptable levels while at the same time offering a large wavelength range, we explore a dark-field digital holographic microscope (df-DHM)[6,7] that measures the complex field of the OV targets using simple optics, followed by computational algorithms to correct for hardware imperfections.[8,9] The capabilities of our digital holographic microscope (DHM) setup are demonstrated by measuring OV on DBO targets.

In DBO, OV targets are used that are composed of two layers of overlapping gratings with a pitch size of the order of the wavelength of light. These overlapping gratings are illuminated resulting in a +1st and −1st diffraction order. For perfect overlap or zero OV, the intensities in the −1st and +1st diffraction orders (I_{-1} and I_{-1}) are the same. In presence of a mismatch in the overlap, a difference in the intensities of the two diffraction orders is present that scales linearly with the OV value as

$$A = I_{+1} - I_{-1} = K \times \text{OV}, \tag{1}$$

where K is an unknown stack-dependent OV sensitivity term. To determine OV in the presence of the unknown K, two pairs of overlapping gratings are used with a known bias of $+d$ and $-d$, respectively (see bottom of Fig. 1(b)). This yields two measured intensity differences

$$A_+ = K \times (\text{OV} + d), \ A_- = K \times (\text{OV} - d). \tag{2}$$

Measuring A_+ and A_- from the two biased gratings, OV is obtained from the relation

$$\text{OV} = d\left(\frac{A_+ + A_-}{A_+ - A_-}\right). \tag{3}$$

In our DHM concept, the dark-field images formed by the +1st and −1st diffraction orders from OV targets are coherently interfered with two reference beams to get two digital holograms on the image sensor.[8] This results in the parallel acquisition of two overlapping holograms using the imaging lens's full numerical aperture (NA). With three 2D Fourier transforms, the complex amplitude and phase of the −1st and +1st order images are retrieved. Promising OV measurements using DHM have already been shown,[8] and even over a broad wavelength range extending from visible to the near-infrared.[10] Image correction by calibrating and correcting aberrations in the imaging lens and digital apodization to reduce cross-talk effects from neighboring structures around OV targets have already been shown.[9,11] We continue to explore various computational
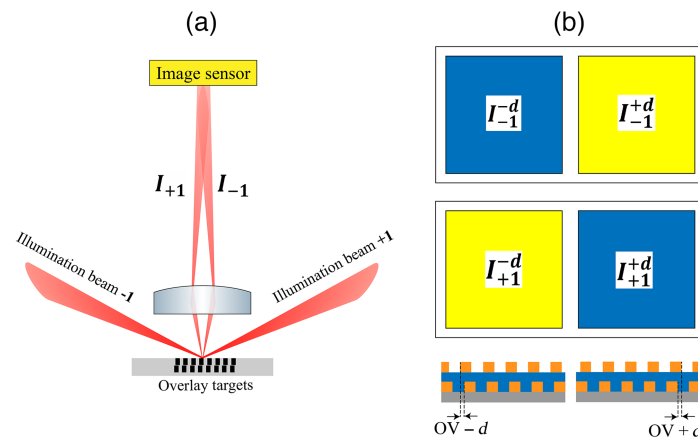

Fig. 1 DBO signal formation. (a) Two illumination beams from opposite angles illuminate the OV targets (biased two-layer gratings) and the two diffraction orders I_{-1} and I_{+1} from each of the two targets constitute the intensities required for OV calculation. (b) Schematic of biased OV targets for DBO. At the bottom, the side views of the double-layer gratings with $-d$ and $+d$ bias are shown, whereas the four intensities I_{-1}^{-d}, I_{-1}^{+d}, I_{+1}^{-d}, and I_{+1}^{+d} are obtained from the images of the targets recorded by the imaging system.

enhancements to this DHM concept that would contribute to more precise and robust OV measurements.

In this paper, we explore the effects of a non-uniform illumination beam profile on the imaging of OV targets and its effect on OV measurements. In DHM, two oblique illuminations are used with the angle of illumination adjusted so that zeroth order diffraction is not captured by the imaging lens. These illumination beams generate a +1st order (coming from one illumination beam) and a −1st order (coming from the other illumination beam). The intensities of the +1st and −1st order beam are

$$I_{+1} = I_{\text{ill}(+1)} \times \text{DE}\left(1 + \frac{K}{2} \times \text{OV}\right), I_{-1} = I_{\text{ill}(-1)} \times \text{DE}\left(1 - \frac{K}{2} \times \text{OV}\right), \quad (4)$$

where $I_{\text{ill}(+1)}$ and $I_{\text{ill}(-1)}$ are the illumination intensities of the two illuminations respectively, and diffraction efficiency (DE) of the grating stacks. Ideally, $I_{\text{ill}(+1)}$ and $I_{\text{ill}(-1)}$ need to be identical in both intensity level and profile, which can be challenging in experiments. If we separately calibrate the individual illumination intensities for the two diffraction orders, then the corrected diffracted intensities from the targets $I_{\pm1}^{\text{corr}} = I_{\pm1}/I_{\text{ill}(\pm1)}$ can be used to determine OV that is independent of the individual intensities of the two arms.

In addition to correcting for the total intensity of each illumination beam, which can be done by deflecting part of the incident light with a beamsplitter into a photodiode, correction for the spatial intensity profile $I_{\text{ill}}(\vec{r})$ is also necessary to eliminate intensity variations within targets. While ideally, the targets would be illuminated by two top-hat uniform beam spots with the same intensity and polarization, it is usually difficult to achieve this in practice. Our DHM concept uses a spatially coherent near-collimated illumination beam from a single-mode (SM) fiber. This results in a Gaussian-like illumination beam profile on the wafer. However, a Gaussian illumination beam profile makes OV metrology sensitive to target positioning errors. In this work, we first calibrate the beam profile of the Gaussian illumination beam using a large diffraction grating and then use the calibrated profile to correct images of OV targets to improve OV accuracy and precision.

In the following sections, we will first briefly introduce the DHM setup, followed by the experimental methods, and results on the calibration of the illumination spot. Later, we will show measurements on OV targets and apply the calibrated spot profiles to correct the target images. We show that OV values extracted from these measurements are clearly improved after the illumination beam spot is corrected, which demonstrates that our beam profile correction method improves the OV metrology precision. We also show that consistent OVs can be measured when targets are placed at different relative locations of the illumination beam.

2 Methods

2.1 Dark-Field Digital Holographic Microscope

Digital holographic microscopy is a coherent imaging system where the reflected or transmitted field from an object (E_{obj}) interferes with a reference field (E_{ref}) to get an interference pattern (I) on the image sensor, called the digital hologram. The intensity pattern of the digital hologram is given by

$$I(\vec{r}) = E_{\text{obj}}(\vec{r})E_{\text{obj}}^*(\vec{r}) + E_{\text{ref}}(\vec{r})E_{\text{ref}}^*(\vec{r}) + \gamma(\vec{r})E_{\text{ref}}(\vec{r})E_{\text{obj}}^*(\vec{r}) + \gamma(\vec{r})E_{\text{obj}}(\vec{r})E_{\text{ref}}^*(\vec{r}), \quad (5)$$

where $E_{\text{obj}}(\vec{r})$ and $E_{\text{ref}}(\vec{r})$ are the complex amplitude distributions of the object and reference at image sensor position $\vec{r}$, respectively, and $\gamma(\vec{r})$ is the degree of coherence between the object beam and the reference beam. The object field is then reconstructed from the hologram with both amplitude and phase information using fast Fourier transforms (FFT).[12]

The schematic of the df-DHM setup, similar to the one described in Ref. 8 is shown in Fig. 2. Figure 2(a) contains the part where spectrally filtered light is split into four parts coupled into four polarization-maintaining (PM) SMs that are used as two pairs of illumination beams and reference beams. First, the broadband output from a supercontinuum source is spectrally filtered by an accousto-optic tunable filter (AOTF) with a bandwidth $\Delta\lambda$ of about 4 nm. The fiber-coupled collimated output from the AOTF is then split into two parts using a non-polarizing 50:50 beam splitter. The coherence length is of the order of 70 μm for visible wavelengths, and
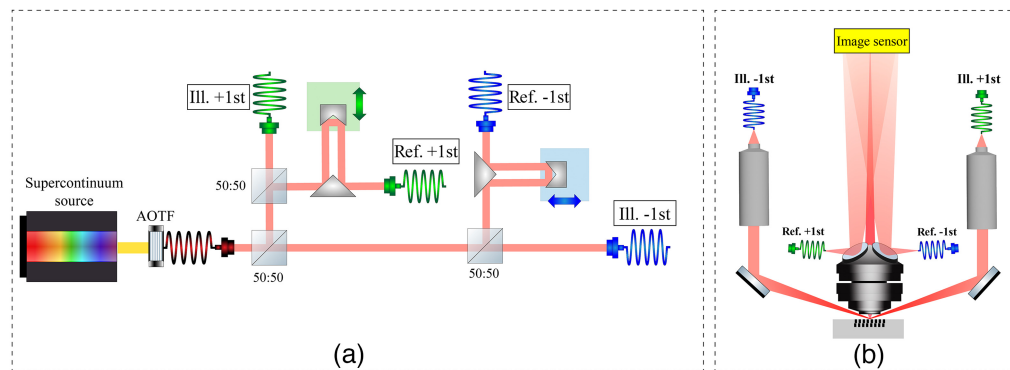
Fig. 2 Schematic of the experimental setup of df-DHM. (a) The output of the supercontinuum source is filtered by the AOTF into quasi-monochromatic radiation with a bandwidth of a few nm. The collimated fiber-coupled AOTF output is then split into two parts, each for one pair of illumination and reference, by a 50:50 beam splitter. Each split beam then goes through another 50:50 beam splitter where one part couples into the illumination fiber and the other into the reference fiber after an adjustable delay line. (b) The DHM sensor: includes two objective lenses to focus the two illumination beams on the target at an oblique incidence. The imaging lens images the targets on the camera, with attached angled mirrors on its outside to direct the reference beams to the camera.

hence the optical path length difference between these two parts is set much longer than the coherence length (a few cm), so that there is no interference between them. Each split beam then goes through another 50:50 beam splitter where one part couples into a fiber for the illumination arm and the other into another fiber for the reference arm via a delay line. As shown in Fig. 2(a), each delay line consists of a 90-deg reflective prism and a hollow roof prism mounted on a linear translation stage with micrometer screws. The outputs of these fibers are then sent to the sensor part of the DHM, which is shown in Fig. 2(b).

OV metrology needs high imaging resolution to separate the target from surrounding patterns. This requires imaging with a high NA, which is difficult to achieve with a lensless setup since this would result in a large angular spread of light beams on the image sensor. Therefore, we use a custom-made imaging lens manufactured by Anteryon that consists of two lens elements, similar to the one described in Ref. 13. The imaging lens has an NA of 0.8, with a sufficiently large free working distance of 2.9 mm to allow the illumination of the target with a collimated off-axis illumination beam. However, with such a large imaging NA, the angular range of the off-axis illumination beam's incident angle has to remain small, which does not allow us to project an ideal top-hat-like illumination spot on the wafer. The output of each of the two SMs for illumination is focused using a pair of lenses and redirected using a silver mirror to illuminate the sample surface at a 70 deg angle of incidence. The NA = 0.8 imaging lens collects the diffracted light beams and redirects them to the image sensor with a 100× magnification, as a result, with a 100× lower angular spread. The imaging lens system has a focal length of 7.2 mm, and thus the image sensor is placed at a distance of slightly more than 720 mm from the lens. In our off-axis DHM concept, the object and reference beams have a sufficiently large angle between them so the interference term $E_{\text{obj}}(\vec{r})E_{\text{ref}}^*(\vec{r})$ can be computationally retrieved using Fourier transform techniques.[14,15] The reference fiber outputs do not have collimating optics, so the diverging beams from the fiber tips propagate in free space to the image sensor after reflecting from the two built-in mirrors on the lens holder, as shown in Fig. 2(b). The image sensor is a 12-bit complementary metal-oxide semiconductor (CMOS) camera (Basler a2A4504-5gm) with a square sensor of 20.2 megapixels, with square pixels of size 2.74 μm.

2.2 Illumination Spot Profile Calibration Using DHM

To measure the illumination beam spot $I_{\text{ill}}(\vec{r})$ as incident on the OV targets, we use a large [much larger than the field-of-view (FoV) of the imaging system and the illumination spot size] grating as a calibration target. Since we are interested in calibrating a beam spot with an oblique incidence (usually 70 deg), the pitch of the calibration grating is chosen in such a way so that with the chosen angle of incidence, the first order diffraction from the grating is perpendicular to the
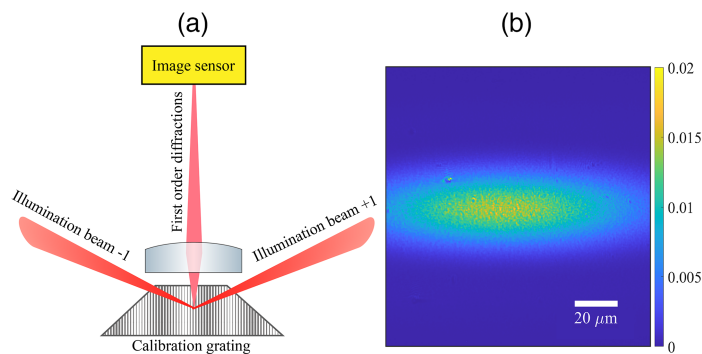
(a)

(b)

Fig. 3 (a) A conceptual schematic of the illumination beam profile calibration for the DHM setup. The calibration target is a large grating that sends the first-order diffracted light to the image sensor through the middle of the imaging lens. The first-order diffracted beams from the two illumination beams coming from opposite directions are overlapped. (b) An intensity image on the camera of the overlapping +1st and −1st orders from the calibration grating produced by two oblique illumination beams from opposite directions.

grating surface. For these experiments, we use a commercially available grating from ThorLabs (GH13-18V—Visible Reflective Holographic Grating, 1800 lines/mm), which corresponds to a pitch size of 555.6 nm. For this pitch size, we choose a wavelength of 522 nm for the experiment, which is the wavelength at which the first order diffraction is normal to the grating surface when the angle of incidence is 70 deg. The first-order diffracted beams for both illumination arms are captured by the imaging lens and they transmit through the center of the exit pupil of the imaging lens, as shown in Fig. 3(a). The diffracted beams are then imaged on the sensor, as seen in Fig. 3(a), which gives expected Gaussian-like beam profiles that are stretched along one direction due to the oblique incidence. In addition to the intensity profile, speckles are also observed that is caused by the optically rough surface of the calibration grating.

The imaged diffracted orders of the calibration grating are the calibrated intensity profiles of the illumination beams, which are overlapping in the FoV of the sensor. However, in our DHM concept, we can retrieve both complex illumination profiles on the grating using the parallel acquisition feature.[16,17] Two overlapping digital holograms of the two illumination beams are created by coherently interfering the diffracted beams with their corresponding reference beams [Fig. 4(a)]. With a 2D FFT, we digitally move to the pupil plane and obtain the baseband containing the first two terms of Eq. (5) and the fully-separated sidebands containing the interference terms and their conjugates for both arms, as shown in Fig. 4(b). In the pupil plane (i.e., each sideband of the frequency spectrum), a central amplitude peak is observed as expected for the diffraction orders. In addition, the whole NA of the lens is also filled with a background with homogenously distributed speckles, originating from the rough sample surface.

Next, with an inverse FFT of the sidebands, we reconstruct the complex field of the two illumination beams, $E^{ill}_{+1}(\vec{r})$ and $E^{ill}_{-1}(\vec{r})$ whose absolute values give the amplitudes [Figs. 4(c), 4(d)] and their arguments give their 2π wrapped phases [Figs. 4(e), 4(f)]. Thus, we obtain the calibrated complex field of the illumination beam spot at a particular wavelength (in this case, 522 nm). Note that the reconstructed intensities, plotted as the square of the absolute values of $E^{ill}_{+1}(\vec{r})$ and $E^{ill}_{-1}(\vec{r})$, are not the same. Later, we show that this calibration step also helps to eliminate the effect of the intensity imbalance between the two arms on OV measurements. It is to be noted that this is a one-time calibration step on a dedicated calibration target that can be placed on a fiducial plate inside the OV metrology tool. For actual on-product OV measurements, the same calibrated beam profiles would be used for correction.

3 Results

3.1 OV Target Measurements With and Without Illumination Profile Correction

After calibrating the complex illumination field, the calibration grating is replaced by a silicon test wafer containing pairs of OV targets of size 38×38 μm^2 with programmed OV values in the range of −20 to 20 nm with a step size of 10 nm. Each target consists of two overlapping grating
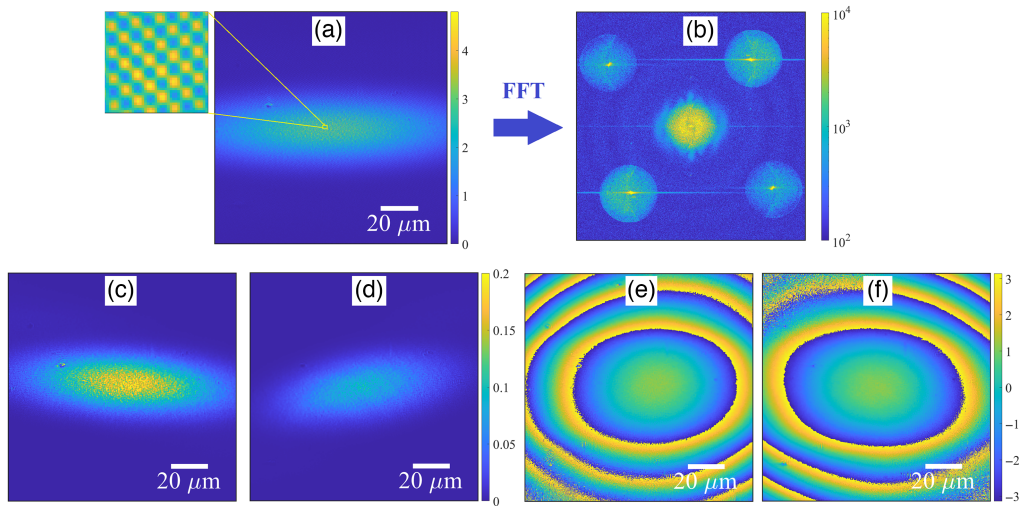
Fig. 4 (a) Recorded overlapped holograms of the +1st and −1st orders of the beams diffracted by the calibration grating. The checkerboard pattern of the zoomed-in part of the digital hologram shows the two sets of interference fringes running in opposite directions diagonally. (b) The spatial frequency of the digital hologram after a 2D FFT, which includes the central baseband containing the non-interfering terms of the object and reference beams and the sidebands containing the interference terms. (c) and (d) The reconstructed intensities and (e) and (f) 2π wrapped phases of the two diffraction orders from the calibration grating.

pairs with an OV bias d of +20 and −20 cm, as shown in the bottom of Fig. 1(b). It is to be noted that we have already reported OV metrology results using DHM on smaller targets of $5 \times 5\ \mu m^2$ using an NA = 0.5 imaging lens[10] and with the NA = 0.8 lens that we now use, we are confident that we can measure on even smaller metrology targets. The OV targets are measured in the DHM following the same procedure as the illumination beam measurement. Digital holograms of the +1st and −1st orders from the targets are recorded and the reconstructed amplitudes of the nine sets of target pairs are shown in Fig. 6(a). The illumination beam spot is clearly visible on the reconstructed intensity images of these large targets. The wrapped phase profile of the target pair shows curved 2π-wrapped phase jumps, implying the presence of a curved phase front. After this, the measured complex fields are corrected by dividing them by the pre-calibrated illumination spot as

$$E^{obj}_{+1(corr)}(\vec{r}) = E^{obj}_{+1}(\vec{r})/E^{ill}_{+1}(\vec{r}), \quad \text{and} \quad E^{obj}_{-1(corr)}(\vec{r}) = E^{obj}_{-1}(\vec{r})/E^{ill}_{-1}(\vec{r}). \tag{6}$$

As seen in Fig. 5, the intensity gets significantly more uniform across each target after this correction step. Moreover, after correction, the 2π-wrapped phase jumps run along straight lines indicating that the phase profile of the corrected target image is a tilted plane wave. This implies that the phase curvature before the correction step originates from the illumination optics, since the curvature gets eliminated in this correction process.

For both corrected and not corrected images of the OV targets, the OV values are calculated using Eq. (3) with $d = 20$ nm. To calculate OV, we use the mean intensity inside a region of interest (RoI) in each square, excluding the edges. The area of this RoI is kept constant for all targets for a fair comparison. The measured mean OVs as a function of the set OVs are plotted in Fig. 6(c). Before illumination spot correction, the OV values are linear with the set values, with an offset of about 20 nm and a slope of 1.57. When the illumination correction is applied, the mean OV values are much closer to the expected values with an offset of only 2.96 nm and the slope improves to 1.08. The OV variations σ plotted in Fig. 6(d) are derived from the pixel-to-pixel intensity variation in a target for two diffraction orders. Illumination spot correction significantly reduces this pixel-to-pixel OV variation to a standard deviation that is < 10 nm. The interesting part of this measurement is its robustness against the intensity imbalance between the two illuminations, as was seen in the reconstructed illumination intensities in Figs. 4(c) and 4(d).

Another effect of the non-uniform illumination spot profile is the variation of the retrieve OV value if the target position relative to the beam spot is changed. With illumination spot correction,
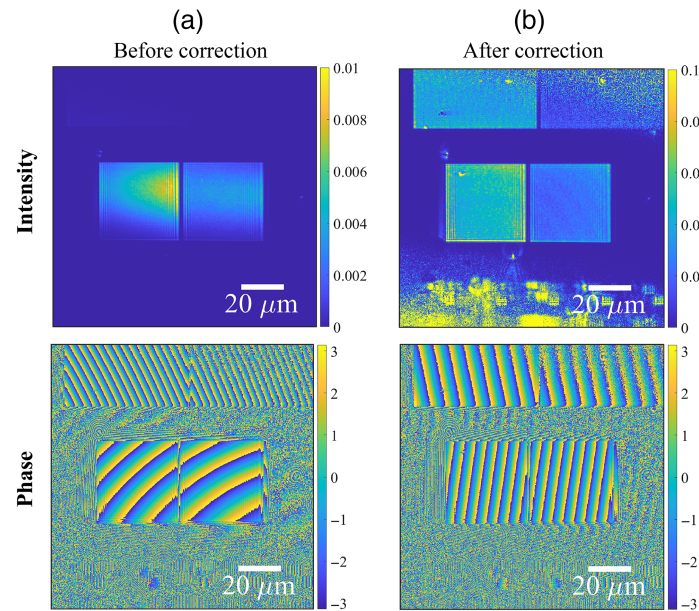
Fig. 5 Reconstructed intensity (top) and 2π wrapped phase (bottom) of the +1 diffraction order for an OV target pair (a) before and (b) after illumination spot correction.
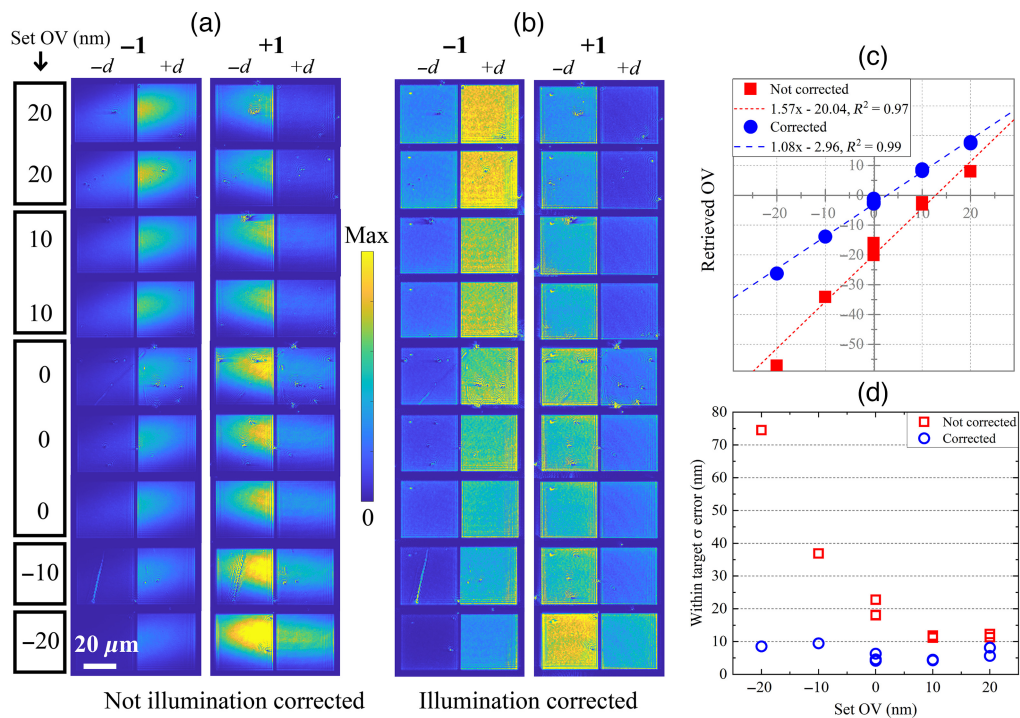

Fig. 6 The holographically reconstructed intensity images of the OV target pairs for both diffraction orders (a) before and (b) after correction of the illumination spot, measured at wavelength 522 nm and bandwidth of a few nm. (c) The estimated mean OV values estimated from uncorrected and corrected images as a function of programmed OVs. (d) Propagated σ error of the OVs derived from the pixel-to-pixel intensity variation in each target for two diffraction orders.

we expect to eliminate this effect. Hence, we check if we achieve more consistent OV values for the same pair of targets at different relative locations within the illumination beam across the FoV. For this, we perform a measurement on one set of OV set-get targets with set OV of 0 nm by translating the targets across the FoV along the horizontal direction, whereas the illumination beams are kept constant. A total of 6 holographic images were captured by translating the stage
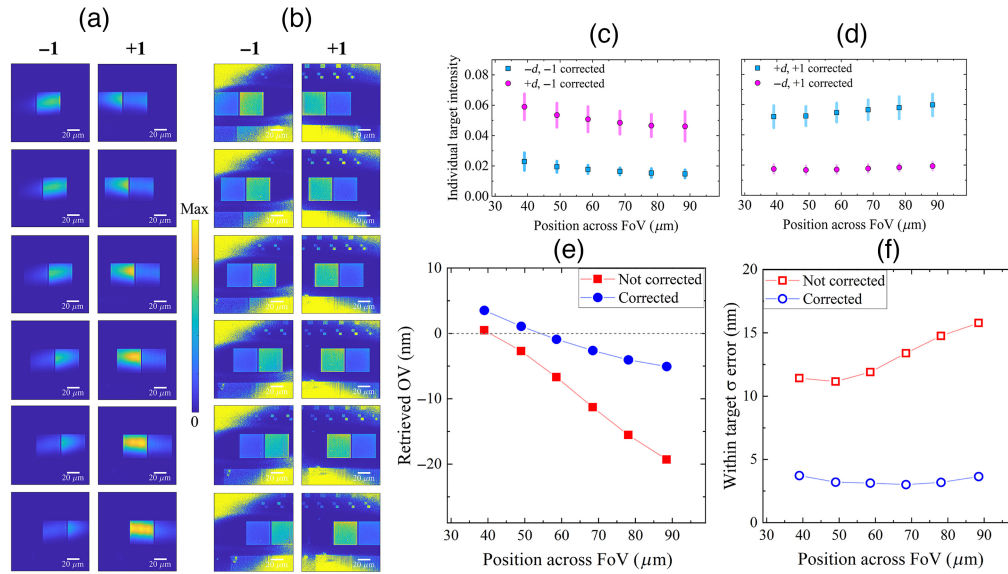
Fig. 7 The −1st and +1st order reconstructed intensity images (a) before and (b) after illumination correction of a pair of OV targets with programmed OV = 0 nm as the targets are moved across the camera FoV from left to right, measured at wavelength 522 nm and bandwidth of a few nm. (c) and (d) The mean corrected intensity of each individual target with their standard deviations as the error bars as a function of horizontal position on the FoV for −1st and +1st diffraction orders, respectively. (e) The extracted OV values and (f) the σ errors propagated from the intensity errors in the targets as a function of position.

with a step size of 10 μm. The reconstructed complex fields are corrected using the calibrated illumination field following the method discussed above. The −1st and +1st order reconstructed intensity images of the targets before and after correction of illumination spot are shown in Figs. 7(a) and 7(b), respectively. The intensity profiles of the targets get significantly more uniform at all the measured locations after the correction steps. To quantify, the mean intensities of each target ($+d$ and $-d$) for the −1st and +1st orders are plotted in Figs. 7(c) and 7(d), respectively, as a function of FoV positions. The error bars on these data are the standard deviations of the intensities within each target. Slow linear intensity shifts with positive and negative slopes are observed for the +1st and −1st orders, respectively as a function of position. Next, the OV values are calculated for each position of the targets and plotted as a function of position in Fig. 7(e) for both uncorrected and corrected cases. Before illumination correction, the OV values for the same pair of targets vary from 0 to −20 nm from left to right, with a steep slope with respect to position on the field, with relatively high standard deviations σ in the range of 11 to 16 nm, shown in Fig. 7(f). After illumination correction, the OV variation with field position is less, with OV values +3 nm on the left and slowly decreasing to −6 nm on the right of the FoV. The OV precision is significantly improved with σ being < 4 nm at all locations. Although illumination correction improves the OV precision, the values are not the same at all measured positions, which is undesired.

To explain the shift in OV across FoV, we explore the possible reason behind this. The effect of field position-dependent amplitude variation in DHM has been explained by van Gardingen-Cromwijk et al.[13] According to this effect, when the source has limited monochromaticity with a bandwidth of several nm, the holographic imaging system's point spread function (PSF) changes from left to right on the FoV. This is explained by a combination of a wavelength-dependent path length variation within the FoV and a wavelength-dependent focus variation of the uncoated imaging lens. Fourier transforming the PSF yields the coherent modulation transfer function (MTF), which describes the spatial frequency response of our DHM setup. It can be shown[13] that for a Gaussian-shaped spectrum of the measurement light with a bandwidth (BW), this MTF is given by

$$\text{MTF}(\rho) = \exp\left[-\left(\frac{\text{BW}}{4}\right)^2 (a_0 + a_4\sqrt{1 - \rho^2 \text{NA}^2})^2\right], \qquad (7)$$

Coherent MTF showing the location of the +1st diffraction order ⊙
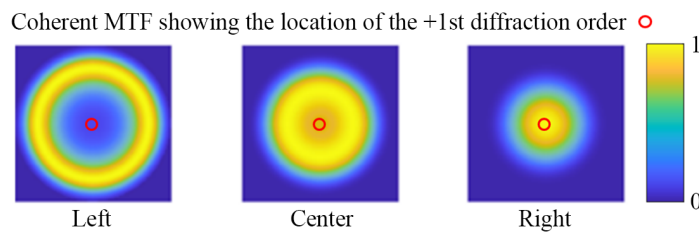

Left   Center   Right

Fig. 8 A qualitative picture that shows how the shape of the MTF changes as one move from left to right in the FoV of our DHM setup. For clarity, the approximate location of the +1st diffraction order of the grating that we used in the experiments has been indicated with a small circle in the center.

where ρ is the normalized radial position in the MTF ($0 \leq \rho \leq 1$). The term a_4 describes the wavelength-dependent focal length of our imaging lens[13] and the term a_0 describes a term that varies linearly with the position in the DHM image field. Qualitatively, we show in Fig. 8 how this MTF varies as one moves from left to right in the image field of our DHM setup. For the sake of clarity, the variation of the MTF in Fig. 8 has been exaggerated. Due to this exaggeration, it can be clearly seen that the transmitted amplitude of the grating varies as the grating is moved from left to right for the +1st diffraction order. The grating signal is attenuated at the left side of the FoV and this grating signal gradually increases as you move the grating to the right side of the FoV. That is why there is an increase in the overall diffracted +1st order intensity of the same target pair from left to right as seen in Fig. 7(d). This effect varies in the opposite direction for the −1st diffraction order in DHM due to the two oblique incidences from opposite directions.

This overall effect introduces an extra intensity imbalance on top of the intensity imbalance caused by the OV, causing inaccuracy in OV measurement when measured at different positions in the field. The illumination spot correction demonstrated here does not eliminate this effect. One easy-to-implement experiment to check if this effect of varying pupil amplitude at different FoV positions can explain the observed residual target position dependency is to use a narrower bandwidth of the source. Decreasing the bandwidth increases the coherence length, thereby reducing the wavelength-dependent effects when one frequency is chosen from the AOTF.

3.2 Robust OV Against Positioning Errors

To check whether the shift in intensity with field position in our experiments is indeed caused by this effect, we perform another experiment using a narrower bandwidth. For these measurements, we used a custom-made calibration grating with a pitch size of 692 nm for the illumination spot correction, which has much lower levels of surface roughness compared to the Thorlabs grating. The wavelength was set at 632.8 nm according to the availability of a narrow-pass filter for this wavelength and is closer to the calibration grating pitch. A laser-line interference filter is used to limit the bandwidth to only 1 nm resulting in a coherence length of about 400 μm, which is long enough compared to the optical path difference (OPD) within the FoV. After calibration of the illumination spot for 1 nm bandwidth, the OV targets are remounted in the setup and the experiments are repeated.

To check whether using a long coherence length gets rid of the spurious apodization effect, the holographic images of one set of targets with set OV = 0 are measured with 1 nm bandwidth at 632.8 nm center wavelength by moving them across the FoV along the horizontal axis. Figure 9(a) show the reconstructed intensities of the −1st and +1st orders of the OV targets from the holograms at six different locations, and Fig. 9(b) shows intensity profiles after being divided by the calibrated illumination spot. The mean intensity and standard deviations of each target are extracted from the corrected intensities and plotted as a function of position in Figs. 9(c) and 9(d). Compared to the position-dependent intensities in Figs. 7(c) and 7(d), the corrected mean intensities here are more constant at every location, with σ error in each target within 7 nm, as seen in Fig. 9(f). On the other hand, we observe large within target σ variations before correction, showing the usefulness of this method. This clearly translates to the calculated OV values and their within target σ in Figs. 9(e) and 9(f). In Table 1, we summarize the mean OV and their standard deviations of all measured positions in the FoV for the two cases with different coherence lengths. The data show a clear improvement in OV precision against target positioning error on the corrected data for the case of 400 μm bandwidth source. The OV variation across a
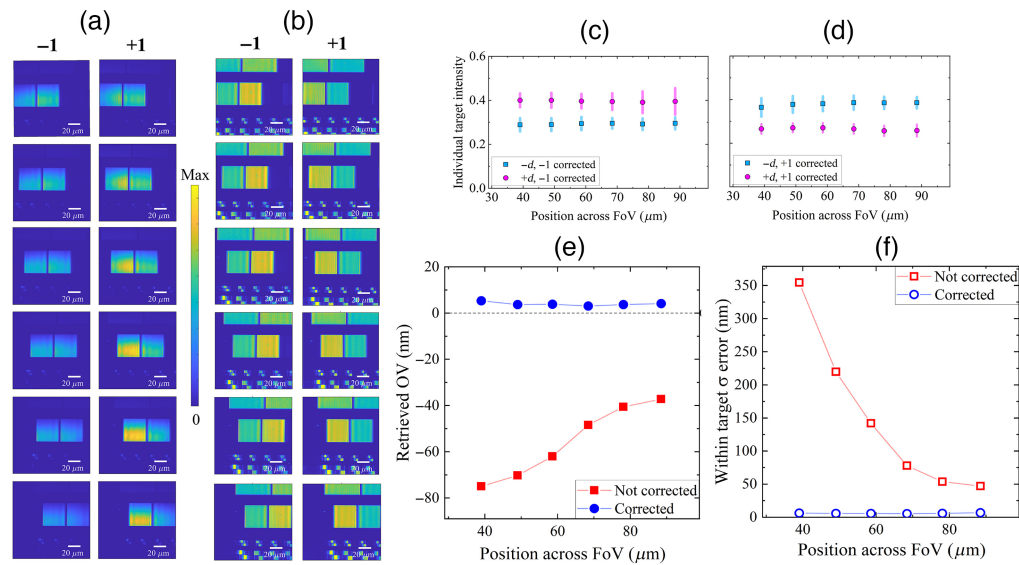
Fig. 9 The −1st and +1st order reconstructed intensity images (a) before and (b) after illumination correction of a pair of OV targets with programmed OV = 0 nm as the targets are moved across the camera FoV from left to right, measured at wavelength 632.8 nm and bandwidth of 1 nm. (c) and (d) The mean corrected intensity of each individual target with their standard deviations as the error bars as a function of horizontal position on the FoV for −1st and +1st diffraction orders, respectively. (e) The extracted OV values and (f) the σ errors propagated from the intensity errors in the targets as a function of position.

Table 1 OV parameters calculated from the position scan experiments.

Wavelength (nm)	Coherence length (μm)	Mean OV (nm)		Standard deviation (nm)	
		Uncorrected	Corrected	Uncorrected	Corrected
522	70	−9.18	−1.33	7.59	3.25
632.8	400	−55.56	3.97	15.76	0.75

relatively large position variation of 50 μm in the FoV, given by the standard deviation of OV values at each location, is only 0.75 nm, as opposed to 3.25 nm for the case of 70 μm bandwidth source.

Next, the holographic images of the other OV targets are also measured and the uncorrected and corrected reconstructed intensity profiles are shown in Figs. 10(a) and 10(b). Note that in this case, the corrected intensity difference between the negatively biased (−d) and positively biased (+d) targets is lower than the case when a wavelength of 522 nm was used. This implies that the OV sensitivity K is lower at 632.8 nm for these targets compared to that at 522 nm. Less sensitivity also implies that OV measurements are more prone to mismatch between the two illumination beams in our DHM setup.

The OV values and their errors within the target are estimated for both non-corrected and corrected cases and are plotted as a function of set OVs in Figs. 10(c) and 10(d). A good linear relation of the measured OV values with the set values after correcting by the illumination spot as opposed to the uncorrected version indicates the effectiveness of this method. The OV offset improves from −54 nm in the uncorrected case to +4 nm in the corrected case. These results indicate that with a sufficient coherence length of the source, consistent OVs can be estimated irrespective of the location of the targets with respect to the illumination beam spot.

The OV offsets of a few nm after the correction could result from a small difference in the angles of incidence of the two illumination beams. Another effect is the polarization state of light used in the measurements. Linearly polarized light is used in the setup coupled into PM SMs.
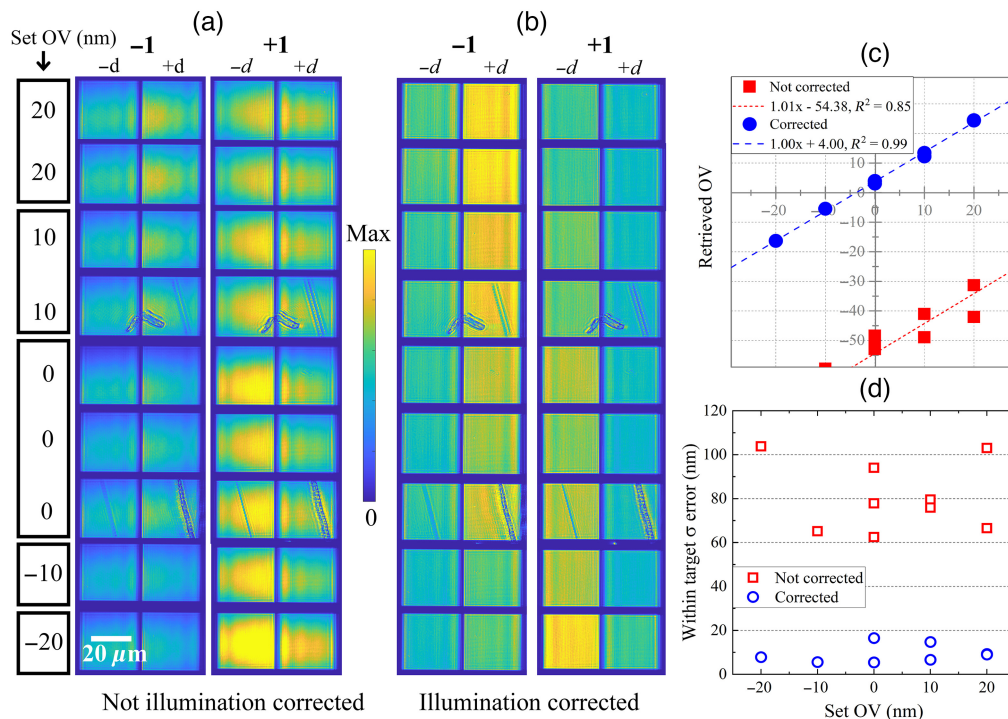
Fig. 10 The holographically reconstructed intensity images of the OV target pairs for both diffraction orders (a) before and (b) after correction of the illumination spot, measured at wavelength 632.8 nm and bandwidth of 1 nm. (c) The estimated mean OV values estimated from uncorrected and corrected images as a function of programmed OVs. (d) Propagated σ error of the OVs from the intensity variation within each target.

Although PM fibers are used, significant polarization crosstalk in such fibers can still be present. Thus, the polarization state after the fibers likely has elliptical components instead of being purely linearly polarized. The orientation of the linear polarization of the two illumination beams is assumed to be the same. Yet, a small difference in the angle of orientation can cause a difference in the DE in the -1st and $+1$st orders.

The larger pixel-to-pixel errors on OV in the case of using 632.8 nm wavelength in Figs. 9(f) and 10(d) as compared to 522 nm Figs. 6(d) and 7(f) are primarily caused by a lower wavelength-dependent stack sensitivity. The targets' stack sensitivity is defined as a ratio of the intensity difference in the $-d$ and $+d$ targets, and their average intensity at $d = 20$ nm and 0 set OV.[18] These values are between 0 and 1, with 0 being the intensity difference between the two targets having no sensitivity to OV shift and 1 being the highest sensitivity. From the experimental data at 632.8 nm, the stack sensitivity is about 0.17, whereas the same targets have a higher stack sensitivity of about 0.51 when 522 nm wavelength was used. Lower sensitivity implies that OV measurements are dependent on lower signal levels and hence more sensitive to imperfections in the measuring system.

4 Discussion

From these results, we see that a significant improvement in OV measurement accuracy and precision is achieved from illumination spot correction. It is very difficult to realize perfectly identical profiles of the two illumination beams on the targets in experiments. Therefore, the illumination spot correction method is very useful when an intensity imbalance is present between the two illumination beams, and both illuminations do not have identical beam profiles. In addition to the intensity profiles, the holographically reconstructed intensities, which are used in DHM to calculate OV, depend on the visibility function γ of the fringes in the FoV. This results in a finite spatial extent of the reconstructed intensity in the FoV, as presented in earlier work on DHM.[19] Since we calibrate the illumination profile with DHM, we also calibrate and correct the visibility at the same time.

One important outcome of the illumination beam profile correction is the robustness against target positioning errors. However, the requirement to realize this in DHM is to be free from the FoV-dependent amplitude variation, as described at the end of Sec. 3.1. We showed that by decreasing the source bandwidth and hence the coherence length, the effect is eliminated and consistent OV values are measured at different locations in the FoV. Another way to get rid of this effect could be by decreasing the angle between the reference and object beams further to decrease fringe density, and hence the number of fringes. However, the consequence of this method is that in Fourier space, the base and the sidebands would partially overlap, and hence separate measurements of the reference and object beams will be required, which would result in longer acquisition times. Alternatively, the observed field-position dependent MTF variation can also be computationally corrected using similar techniques as used for 4D aberration correction that has been reported in Ref. 20.

To put the DHM approach into the perspective of traditional DBO measurements, we discuss the photon budget and cost of computational metrology. Our df-DHM concept is approximately as light-efficient as traditional OV metrology tools. The measurement spot is somewhat larger resulting in a smaller fraction of the light on the metrology targets. However, this is compensated by the fact that our df-DHM concept uses fewer optical elements resulting in lower light losses inside the sensor. These effects roughly compensate each other resulting in comparable acquisition times. The other item concerns the speed of the computations needed for the computational image retrieval and correction. These computations mainly involve 2D FFTs that can ultimately run on fast hardware platforms like GPUs. The calculation times of FFTs on these optimized hardware architectures are in the millisecond range and this can run concurrently with a wafer stage move in a df-DHM metrology tool.

5 Conclusion

Illumination spot correction is one of the many correction techniques that can be applied in DHM for robust OV metrology. With the breadboard setup of DHM, we show significant improvement in the accuracy and precision of OV measurements when the non-uniform illumination beam profiles were corrected following careful calibration steps. To use the full potential of DHM for OV metrology, combining illumination spot correction with computational lens aberration correction methods with a large tunable wavelength range, most experimental imperfections on OV measurement are expected to be resolved computationally using DHM.

References

1. M. Adel et al., "Optimized overlay metrology marks: theory and experiment," *IEEE Trans. Semicond. Manuf.* **17**(2), 166–179 (2004).
2. W. Yang et al., "Novel diffraction-based spectroscopic method for overlay metrology," *Proc. SPIE* **5038**, 200–207 (2003).
3. P. Leray et al., "Diffraction based overlay metrology: accuracy and performance on front end stack," *Proc. SPIE* **6922**, 69220O (2008).
4. M. Adel et al., "Diffraction order control in overlay metrology: a review of the roadmap options," *Proc. SPIE* **6922**, 692202 (2008).
5. K. Bhattacharyya et al., "New approaches for scatterometry-based metrology for critical distance and overlay measurement and process control," *J. Micro/Nanolithogr. MEMS MOEMS* **10**(1), 013013 (2011).

6. E. Cuche, F. Bevilacqua, and C. Depeursinge, "Digital holography for quantitative phase-contrast imaging," *Opt. Lett.* **24**, 291–293 (1999).
7. F. Dubois and P. Grosfils, "Dark-field digital holographic microscopy to investigate objects that are nano-sized or smaller than the optical resolution," *Opt. Lett.* **33**, 2605–2607 (2008).
8. C. Messinis et al., "Diffraction-based overlay metrology using angular-multiplexed acquisition of dark-field digital holograms," *Opt. Express* **28**(25), 37419–37435 (2020).
9. C. Messinis et al., "Aberration calibration and correction with nano-scatterers in digital holographic microscopy for semiconductor metrology," *Opt. Express* **29**, 38237–38256 (2021).
10. T. T. M. van Schaijk et al., "Diffraction-based overlay metrology from visible to infrared wavelengths using a single sensor," *J. Micro/Nanopatterning, Mater. Metrol.* **21**(1), 014001 (2022).
11. C. Messinis et al., "Pupil apodization in digital holographic microscopy for reduction of coherent imaging effects," *Opt. Contin.* **1**, 1202–1217 (2022).
12. U. Schnars and W. Jüptner, "Direct recording of holograms by a CCD target and numerical reconstruction," *Appl. Opt.* **33**, 179–181 (1994).
13. T. van Gardingen-Cromwijk et al., "Field-position dependent apodization in dark-field digital holographic microscopy for semiconductor metrology," *Opt. Express* **31**, 411–425 (2023).
14. D. P. Kelly et al., "Resolution limits in practical digital holographic systems," *Opt. Eng.* **48**(9), 095801 (2009).
15. E. Cuche, P. Marquet, and C. Depeursinge, "Spatial filtering for zero-order and twin-image elimination in digital off-axis holography," *Appl. Opt.* **39**, 4070–4075 (2000).
16. R. Dändliker, E. Marom, and F. M. Mottier, "Two-reference-beam holographic interferometry," *J. Opt. Soc. Am.* **66**, 23–30 (1976).
17. N. Verrier and M. Atlan, "Off-axis digital hologram reconstruction: some practical considerations," *Appl. Opt.* **50**, H136–H146 (2011).
18. K. Bhattacharyya et al., "A complete methodology towards accuracy and lot-to-lot robustness in on-product overlay metrology using flexible wavelength selection," *Proc. SPIE* **10145**, 101450A (2017).
19. C. Messinis et al., "Impact of coherence length on the field of view in dark-field holographic microscopy for semiconductor metrology: theoretical and experimental comparisons," *Appl. Opt.* **59**, 3498–3507 (2020).
20. W. M. Coene et al., "Computational imaging for correction of non isoplanatic aberrations in optical wafer metrology," in *MathMet Int. Conf.* (2022).

Manashee Adhikary received her BS and MS degrees in physics from Gauhati University, India, in 2014 and 2016, respectively, and her PhD in nanophotonics from the University of Twente in 2021. She is a postdoctoral researcher at Advanced Research Center for Nanolithography (ARCNL), and Vrije Universiteit, Amsterdam. Her interests include optical metrology techniques, digital holography, imaging, and light scattering applications.

Tamar van Gardingen-Cromwijk received her BSc and MSc degrees in applied physics from Eindhoven University of Technology. She is currently pursuing a PhD at ARCNL in Amsterdam and Vrije Universiteit, Amsterdam. The goal of her PhD research is the development of a metrology tool based on holography, capable of robust semiconductor metrology with the aid of computational algorithms.

Jo de Wit joined Advanced Semiconductor Materials Lithography (ASML) in 2007, and currently he is a senior researcher since 2021. His research interests include optical designing, meta-lenses, and metrology.

Stefan Witte received his BSc degree in applied physics from Hogeschool Eindhoven in 1987 and his PhD from Vrije Universiteit, Amsterdam, in 2007. He is a group leader of the EUV Generation and Imaging Group at ARCNL, head of the ARCNL Metrology Department, and associate professor at Vrije Universiteit, Amsterdam. His research interests include coherent diffractive imaging with visible and EUV radiation, high-harmonic generation and its applications, photoacoustic imaging, and advanced laser development for plasma experiments.

Johannes F. de Boer received his PhD in experimental optics from the University of Amsterdam in 1995. He is a full professor and department head of Physics and Astronomy Department of the Vrije Universiteit, Amsterdam. His research focuses on optical coherence tomography and light interferometry for biomedical imaging and metrology in scattering samples, and the characterization of local polarization properties.

Arie den Boef received his BSc degree in electrical engineering from the Eindhoven Polytechnic Institute in 1985 and his PhD from the University of Twente in 1991. He worked at Philips from 1979 to 1997 where he worked in the areas of laser diodes, optics, MRI, and optical storage. He joined ASML in 1997, where he explored various optical metrology techniques. He is also a part-time full professor at Vrije Universiteit Amsterdam and leads the group of Computational Imaging at ARCNL.